



# Effect of heat treatments and loading orientation on the tensile properties and fracture toughness of AlSi7Mg alloy produced by Laser Powder Bed Fusion

João Teixeira Oliveira de Menezes · Enrique Mariano Castrodeza ·  
Luca Patriarca · Riccardo Casati

Received: 9 December 2021 / Accepted: 25 March 2022  
© The Author(s) 2022, corrected publication 2022

**Abstract** The present study investigates the effect of building orientation and heat treatment routes on the mechanical behavior of the AlSi7Mg alloy (A357) produced by Laser Powder Bed Fusion. The microstructure and mechanical behavior of A357 in the as built, T5 (directly aged) and T6 (solution treated, water quenched and aged) conditions were compared. Tensile properties of the material were evaluated along two main directions (parallel and normal to the building platform), whereas fracture toughness was measured with cracks placed in three orthogonal orientations. The results indicate that the anisotropy in mechanical properties is greatly reduced after T6 temper, but the selection of the best condition between the as built, T5 and T6 temper must consider the main loading directions and possible crack growth orientations associated with the specific application.

**Keywords** Fracture toughness · *J*-*R* curves · Laser Powder Bed Fusion · A357 Al alloy · T6 thermal treatment

## 1 Introduction

Additive Manufacturing (AM) processes enable to produce parts starting from 3D digital models, through a layer-by-layer deposition of material, allowing the fabrication of complex-shape parts for structural and functional applications. Nowadays, several industries in the biomedical, aerospace, automotive, nuclear, and petrochemical sectors adopted the Laser Powder Bed Fusion (LPBF) AM process to produce components (Aboulkhair et al. 2019; DebRoy et al. 2018; Gu et al. 2012). The LPBF process features a laser beam to melt a metal powder bed selectively (BS En ISO/ASTM 2017). The overlapping of melt pools and layers induces successive heating and cooling cycles in the solidified material leading to the formation of complex microstructures. To enhance and fine-tune the material properties it is important to further modify the microstructure by proper thermal treatments.

One of the alloys that found major success in the last decade is the AlSi7Mg (A357) which is nowadays largely used for structural parts produced by LPBF thanks to its good processability, corrosion resistance and high ratio between mechanical performances and density. The A357 is a heat-treatable hypoeutectic alloy mainly strengthened by Mg-Si-Al precipitates ( $\beta''$ ) formed during artificial aging (Handbook 1992; Ninive et al. 2014). In some cases, the high cooling rates involved in the LPBF process leads to the formation of supersaturated solid solutions, and this

---

J. T. O. de Menezes · E. M. Castrodeza ·  
L. Patriarca · R. Casati (✉)  
Department of Mechanical Engineering, Politecnico di  
Milano, Via G. La Masa 34, 20156 Milano,  
MI, Italy  
e-mail: riccardo.casati@polimi.it

opens new possibilities to perform optimized aging treatments after manufacturing (Fiocchi et al. 2021). In our previous work (Menezes et al. 2019), it was noticed that the A357 alloy produced by LPBF shows high mechanical anisotropy, especially in terms of fracture toughness, when it is tested in as built (AB) and directly aged (T5) conditions. Consequently, the T6 temper (i.e. solution heat treatment, water quenching and artificial aging), which is widely performed in cast A357 part, is here proposed as a feasible heat treatment route to reduce material anisotropy. Indeed, the high temperature solution treatment is believed to be able to homogenize the microstructure and consequently reduce mechanical properties. Thus, with this work, the mechanical behavior of the AB, T5 and T6 A357 alloy processed by LPBF in terms of fracture toughness and tensile properties was investigated.

The tensile mechanical properties were assessed along the direction orthogonal and parallel to the building direction, whereas the fracture toughness, evaluated through crack-growth resistance curves ( $J$ -R curves), was determined from specimens with cracks in three orthogonal orientations, associated with the same main directions. To investigate the crack path in the different crack plane orientations and microstructural features, analyses were carried out using optical, scanning and transmission electron microscopes.

## 2 Experimental

### 2.1 Raw material, processing, and thermal treatments

The specimens were printed from gas atomized A357 Al alloy powder supplied by LPW South Europe Srl. According to the information given by the supplier, the size distribution of the powder was within the range 20–63  $\mu\text{m}$ . The chemical composition of the A357 powder is reported in Table 1.

**Table 1** Chemical composition (weight fraction, %) of the A357 Al powder

Si	Mg	Fe	Cu	Mn	N	O	Al
6.5	0.58	0.1	< 0.05	< 0.1	< 0.2	0.1	Balance

The LPBF parameters were optimized to obtain high density material and to minimize the presence of defects. The process was carried out under Ar atmosphere by a Renishaw AM250 system that uses a single mode pulsed-wave fiber laser. The processing parameters that were used to build the specimens are collected in Table 2. Samples for tensile and fracture toughness tests were produced using a meander scanning strategy and the scanning direction was rotated by  $67^\circ$  after each layer completion.

The produced specimens were tested in three metallurgical conditions: i) AB, ii) after T5 temper and iii) T6 temper. For the T5 condition, AB specimens were directly aged at 160  $^\circ\text{C}$  for 4 h (Casati and Vedani 2018). The T6 temper consisted of a solution heat treatment at 540  $^\circ\text{C}$  for 1 h followed by water quenching and aging at 160  $^\circ\text{C}$  for 4 h (Casati and Vedani 2018).

### 2.2 Mechanical testing

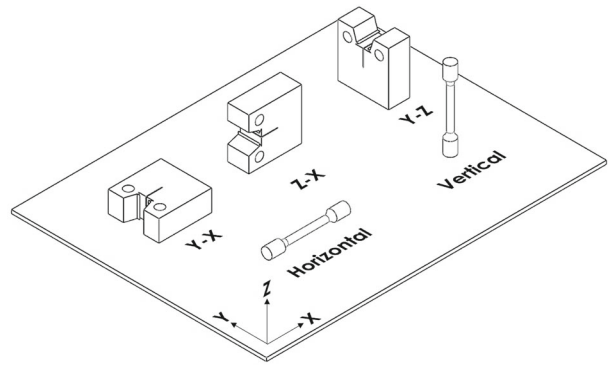
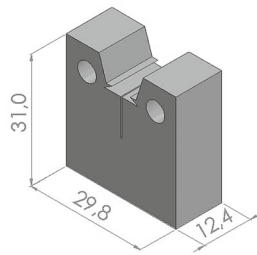
Specimens for tensile tests were machined from printed bars with dimensions of  $10 \times 10 \times 100 \text{ mm}^3$ . Tensile specimens printed orthogonally to the building direction were labelled as H (horizontal), while specimens aligned to the building direction were named as V (vertical) (see Fig. 1). Tensile tests were performed according to the ASTM E8/E8M-21 standard (ASTM E8, E8M-21 2021) in air at room temperature, under constant crosshead speed of 0.5 mm/min. Three specimens were tested for each direction and material condition.

Fracture toughness tests according to ASTM E1820-20 standard (ASTM E1820-20b 2020) were performed on C(T) specimens with nominal dimensions of  $W = 24.8 \text{ mm}$  and  $B = 12.4 \text{ mm}$ . According

**Table 2** LPBF processing parameters

Parameter	Setting
Laser power	200 W
Point distance	80 $\mu\text{m}$
Hatch distance	115 $\mu\text{m}$
Exposure time	140 $\mu\text{s}$
Focal point (above the powder bed)	1 mm
Layer thickness	25 $\mu\text{m}$

**Fig. 1** Geometry of fracture C(T) and tensile specimens and specimen orientation according to the coordinate system defined by ISO/ASTM 52,921:2013 standard (ISO, ASTM52921-13, Standard Terminology for Additive Manufacturing - Coordinate Systems and Test Methodologies. 2019)



to the ISO/ASTM 52,921:2013 standard (ISO, ASTM52921-13, Standard Terminology for Additive Manufacturing - Coordinate Systems and Test Methodologies. 2019), the Z axis was defined as the building direction, the X axis was defined parallel to the front of the machine, and the Y axis was defined perpendicular to the Z and X axes. The orientation of the coordinate system, used as reference for the crack orientation, is shown in Fig. 1. Depending on the crack orientation, fracture specimens were named as Y-X, Z-X and Y-Z, following the nomenclature of the ASTM E1820-20 standard (ASTM E1820-20b 2020). It is important to note that, although for Y-X and Y-Z specimens the crack plane is the same, the crack extension occurs in perpendicular orientations. Both fatigue pre-cracking and fracture toughness tests were carried out at room temperature, with an MTS Landmark servo-hydraulic testing machine instrumented with a  $\pm 15$  kN load cell and an MTS 632.02F-20 fracture extensometer. The unloading compliance method was used for crack length measurement during specimen loading. For a clear identification of the final crack length after the fracture toughness tests, the specimens were further loaded under fatigue cycles to precisely mark and distinguish the stages of crack extensions. The initial and final crack lengths were measured according to the 9-point average method described in BS 7448-1:1991 standard (BS 1991).

### 2.3 Microstructural and fractographic analyses

The microstructure and the fracture surfaces were analyzed using a light optical microscope (LOM) and

a scanning electron microscope (SEM, mod. Zeiss EVO 50) equipped with energy dispersive X-ray analysis (EDX), secondary electrons and backscattered electrons detectors, and an electron backscattered diffraction (EBSD) detector. Standard grinding and polishing procedures were carried out to prepare samples for metallographic analyses. Chemical and electrolytic etching using Keller's and Barker's reagents, respectively, were performed to reveal the microstructural features. For the EBSD analysis, the specimens were grinded up to 2500 grit sandpaper, polished using diamond pastes and by colloidal silica in a Struers Tegramin machine. To investigate the crack paths through the microstructure, the C(T) specimens were cut orthogonally to the crack plane at half the specimen thickness. After that, the cut surfaces were subsequently grinded, polished, and etched using Keller's solution. Quantitative metallography for specimens in the T6 condition was carried out using the analysis tools of Image J software, where Si particles were analyzed according to the following parameters: average perimeter ( $\mu\text{m}$ ), average area ( $\mu\text{m}^2$ ), circularity, aspect ratio, and average distance between each Si particle ( $\mu\text{m}$ ) estimated considering the particles as perfect circumferences. In addition, TEM analysis was carried out using a Philips CM12 transmission electron microscope operating at 120 kV and equipped with an energy-dispersive X-ray spectroscopy system. Samples were grinded to about  $30 \mu\text{m}$  in thickness by abrasive papers and then polished with diamond paste and silica suspension. Final thickness reduction was achieved by ion milling.

### 3 Results

#### 3.1 Microstructure analysis

Figure 2a shows an optical micrograph of the section parallel to the building direction of an AB sample. The microstructure is composed of tiny solidified melt pools and coarse columnar grains oriented along the main temperature gradient. At higher magnifications, the FE-SEM images of Fig. 2b and the TEM image of Fig. 2c reveal cellular grain growth mechanism. Grains are indeed made up of elongated cells with sub-micrometer dimension decorated at boundary by fine continuous eutectic Al-Si network.

In Fig. 3, TEM images of the A357 directly aged from the AB condition (T5 temper) are reported. Artificial aging performed at 160 °C leads to a slight coarsening of the Al cells (Fig. 3a). At higher magnification (Fig. 3b), it is possible to notice abundant lath-shaped  $\beta''$  ( $Mg_4Al_3Si_4$ ) particles with an average length of about 20 nm that precipitated during aging from the supersaturated solid solution induced by rapid solidification and cooling. Direct aging has also a slight effect on the morphology of Si network at cell boundaries, which become discontinuous (Fig. 3c).

The optical and SEM micrographs of Fig. 4 show the microstructure of T6 samples, i.e. samples that were solution treated at 530 °C and aged at 160 °C. Micro-sized Si particles are dispersed in Al grains. Results of image analysis performed on micrographs of T6 samples are shown in Table 3. As presented in

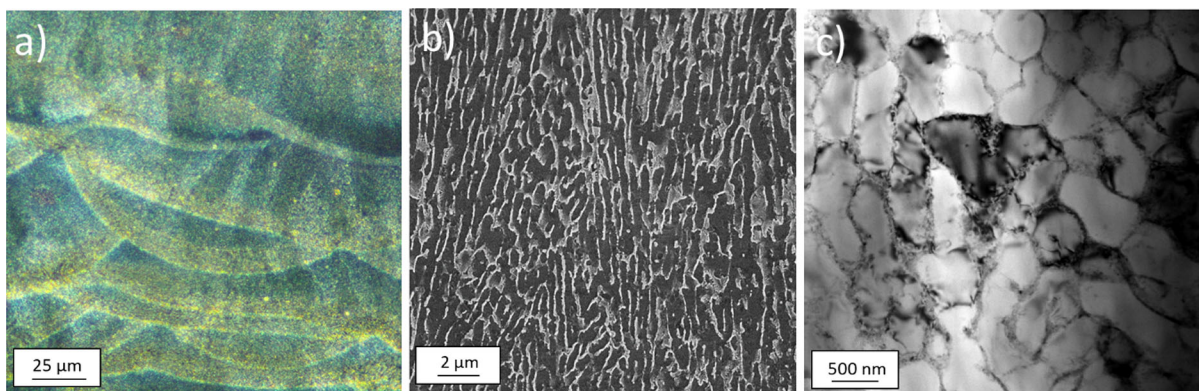
Asghar et al. (2020), the T6 temper leads to precipitation of  $\beta''$  as those shown in Fig. 3 for the T5 temper specimens.

EBSD analyses were performed on the cross section of the building direction for the specimens in the AB and T6 conditions. The orientations map of  $\alpha$ -Al phase for both conditions are reported in Fig. 5a and b, respectively. Elongated grains growing along the building direction without a marked preferred orientation are noticeable. The micrographs show columnar grains growing epitaxially along the thermal gradient from the melt pool boundaries. Similar results are reported in Yang et al. (2018).

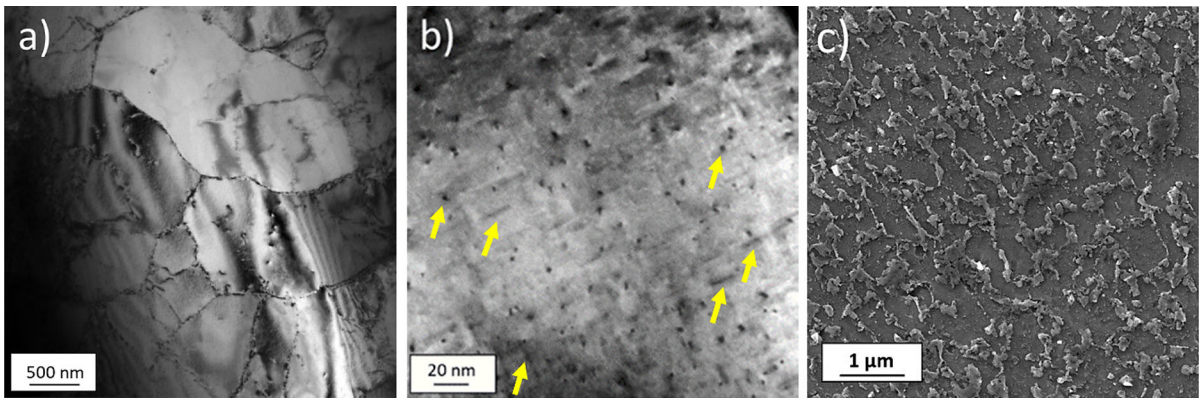
#### 3.2 Tensile tests

Figure 6 presents the tensile stress–strain curves of the A357 alloy in the T6 condition compared with the results of the AB and T5 alloy, previously published in Menezes et al. (2019). From these results the mechanical properties reported in Table 4 were determined.

It is observed from the data reported in Table 4 that the yield stress is severely affected by the T5 temper, while the ultimate tensile stress did not show such pronounced increase. On the other side, the T5 temper heavily decreases the ductility for both the H and V directions. The T6 leads to lower ultimate tensile stresses, while the average yield stress, between H and V directions, is observed to reach an average value of 240 MPa. Remarkably, the ductility of the T6 V specimens is shown to increase with respect to both the AB and T5 conditions.



**Fig. 2** Microstructure of the A357 Al alloy in the AB condition: **a** optical micrograph, **b** FE-SEM image after chemical etching with Keller's solution (section parallel to the building direction), **c** bright field TEM image (section orthogonal to the building direction)



**Fig. 3** Images of the A357 Al alloy after direct aging (T5 temper). **a** TEM image of slight coarsened Al cells, **b** TEM micrograph showing the lath-shaped  $\beta''$  ( $Mg_4Al_3Si_4$ ) particles

(indicated by arrows), and **c** SEM image showing discontinuous Si network at cell boundaries

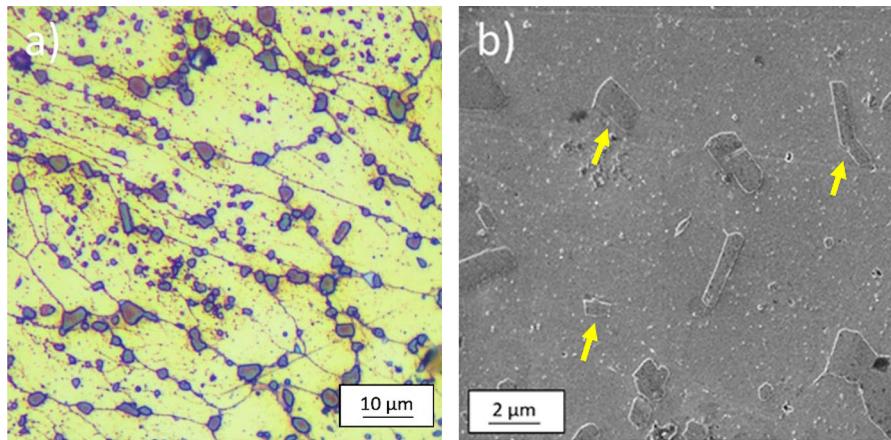


**Fig. 4** Micrographs showing the microstructure of the A357 Al alloy in the T6 condition. **a** Optical micrograph showing the  $\alpha$ -Al grains (light constituent) and the Si particles (dark

constituents) and **b** SEM micrograph showing the Si particles (some of them indicated by arrows)

**Table 3** Geometrical features of the Si particles after the T6 thermal treatment

Feature	Experimental value
Average perimeter ( $\mu m$ )	$3.12 \pm 4.41$
Average area ( $\mu m^2$ )	$1.09 \pm 2.36$
Circularity	$0.81 \pm 0.19$
Aspect ratio	$1.49 \pm 0.66$
Average distance from each Si particle ( $\mu m$ )	$1.89 \pm 0.27$

### 3.3 Fracture tests

Figures 7, 8, and 9 show the Load vs. Crack Mouth Opening Displacement ( $P$ -CMOD) records for the C(T) specimens tested in the AB, T5 and T6 conditions, respectively. The unloading–reloading

sequences necessary for crack extension measurement by the elastic unloading compliance technique are noticeable in the experimental records. Additionally, Fig. 10 shows representative images of the fracture surfaces of the C(T) specimens for each condition. In these images it is clear to observe, from the top to the

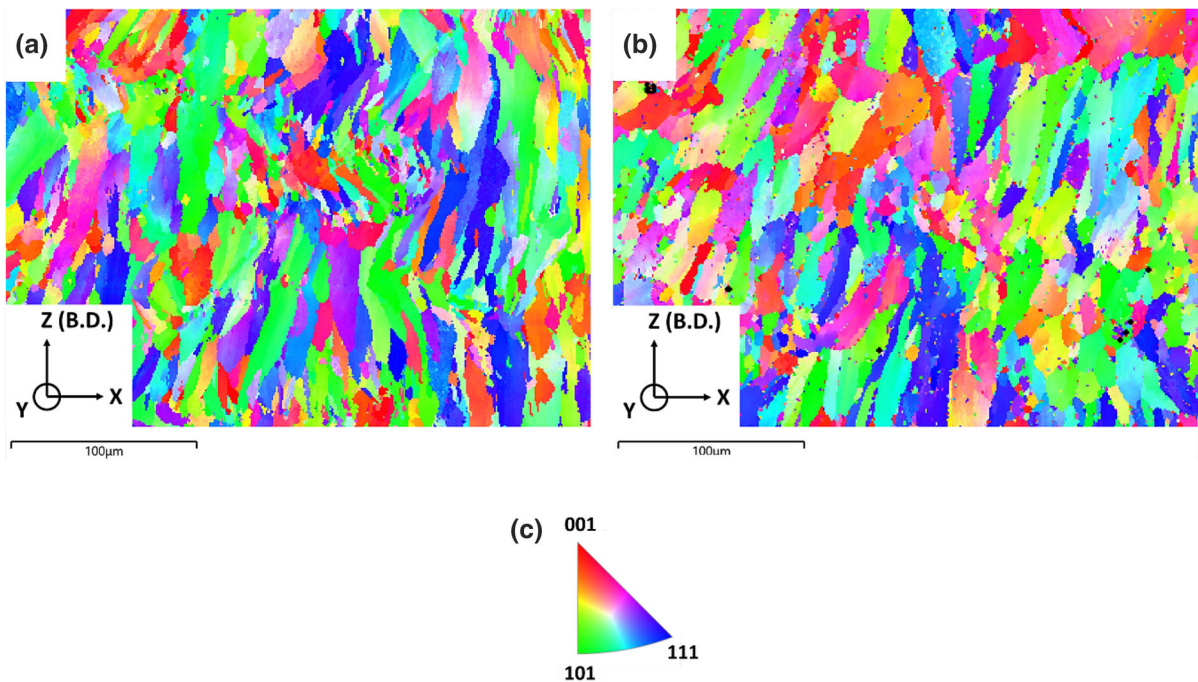


**Fig. 5** EBSD diagrams of a) AB A357 alloy sample, b) T6 temper A357 alloy sample, and c) Representation of the color code used to identify the crystallographic orientations

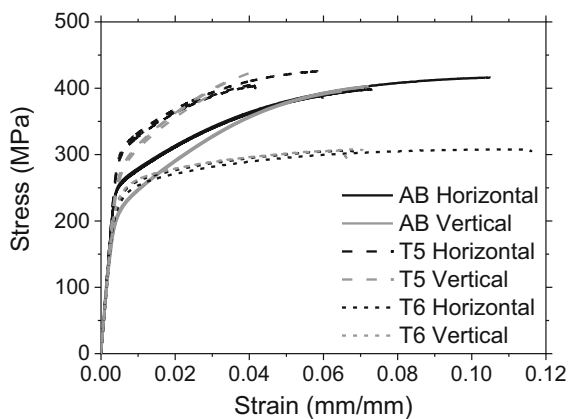


**Fig. 6** Stress vs. strain records for the horizontal and vertical specimen of A357 Al alloy in the AB, T5 and T6 conditions

bottom, the notch, the fatigue pre-crack, the stable crack growth, and the fatigue post-crack regions.

### 3.4 Crack growth resistance curves and fracture toughness

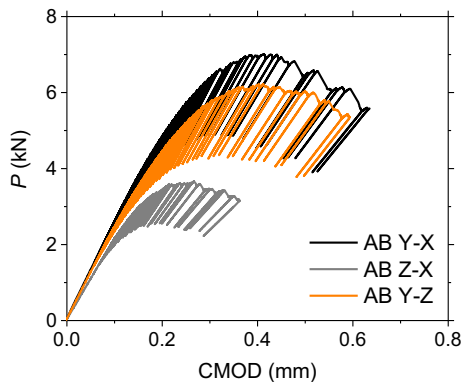
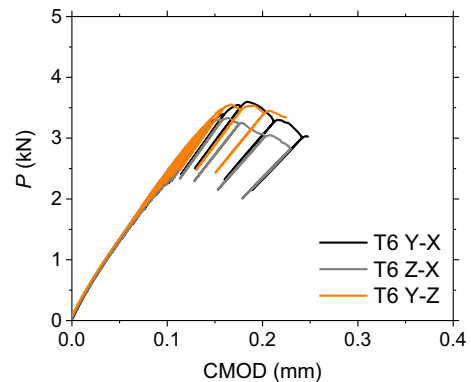
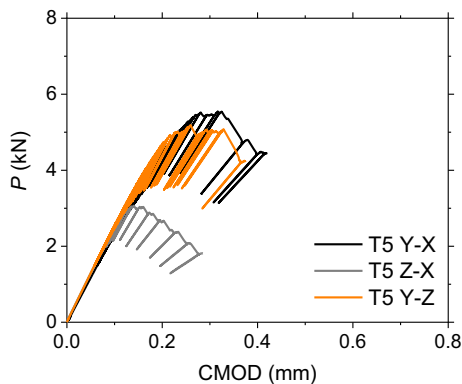
The adjusted  $J$ - $R$  curves obtained from the experimental  $J$ - $\Delta a$  pairs of points for the T6 specimens in the three different crack propagation orientations are shown in Fig. 11 and compared with results of AB and T5 conditions from Menezes et al. (2019), where the blunting line and the 0.2 mm offset line were also reported. Fracture toughness values ( $J_{Ic}$ ) were determined from the intersection of the  $J$ - $R$  curves with the 0.2 mm offset line parallel to the blunting line, according to the ASTM E1820-20b standard (ASTM E1820-20b 2020). The experimental  $J_{Ic}$  values for all the tested specimens are reported in Table 5.

### 3.5 Fractographic analysis

The analysis of the fracture surfaces was performed by SEM and images of selected samples are presented in Fig. 12. The micrographs show the fracture surfaces of the fatigue pre-cracked and the stable crack growth regions of the T6 Z-X specimen, both showing dimples, i.e. typical features of ductile fracture.

**Table 4** Tensile properties of the A357 Al alloy for the horizontal and vertical orientations in the AB, T5 and T6 conditions

Condition	Orientation	$\sigma_{YS}$ (MPa)	$\sigma_{UTS}$ (MPa)	$\sigma_{YS}/\sigma_{UTS}$	Elongation at break [%]
AB (Menezes et al. 2019)	Horizontal	$257 \pm 03$	$398 \pm 13$	0.65	$7.6 \pm 1.8$
	Vertical	$216 \pm 02$	$400 \pm 04$	0.54	$6.9 \pm 0.4$
T5 (Menezes et al. 2019)	Horizontal	$309 \pm 03$	$411 \pm 10$	0.75	$4.8 \pm 0.8$
	Vertical	$282 \pm 01$	$411 \pm 21$	0.69	$4.1 \pm 0.4$
T6	Horizontal	$236 \pm 04$	$306 \pm 01$	0.77	$6.8 \pm 0.3$
	Vertical	$245 \pm 01$	$307 \pm 01$	0.80	$9.2 \pm 2.4$

**Fig. 7** P-CMOD records for the C(T) specimens in the AB condition**Fig. 9** P-CMOD records for the C(T) specimens in the T6 condition**Fig. 8** P-CMOD records for the C(T) specimens in the T5 condition

LOM and SEM micrographs of the etched C(T) specimens were taken from the mid-sections perpendicular to the crack plane in the pre-crack and stable crack growth regions. Representative images for the C(T) specimens in the AB and T5 conditions were already presented in Menezes et al. (2019).

Figure 13 shows the crack path of the T6 Y-Z specimen during the fatigue pre-crack and the stable crack-growth regions. From left to right: fatigue pre-crack region, fatigue pre-crack tip (indicated by an arrow) and stable crack growth region. In its turn, Fig. 14 presents in detail the crack path for the T6 Y-X specimen during the stable crack-growth region.

From these images it can be noticed that the crack propagated by connecting pores that are present in the material. Moreover, cracks mostly propagated around Si particles, at boundary between matrix and such second phases, and broken particles are also found seldomly, on crack path and in regions close to the crack (see Fig. 15).

#### 4 Discussion

As can be seen in Fig. 2a, in the AB condition the A357 Al alloy features aligned solidification tracks typical of alloys produced by LPBF. Regions with

**Fig. 10** Representative images of fracture surfaces of the C(T) specimens in the three conditions: AB, T5 and T6

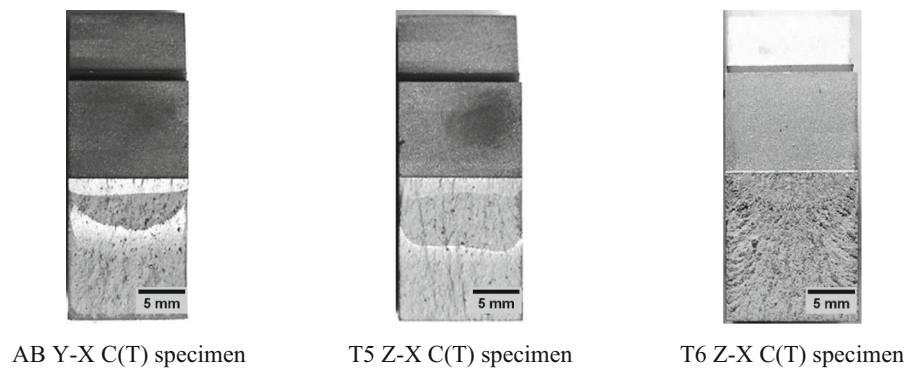


**Fig. 11** J-R curves for the A357 C(T) specimens in the AB, T5 and T6 conditions

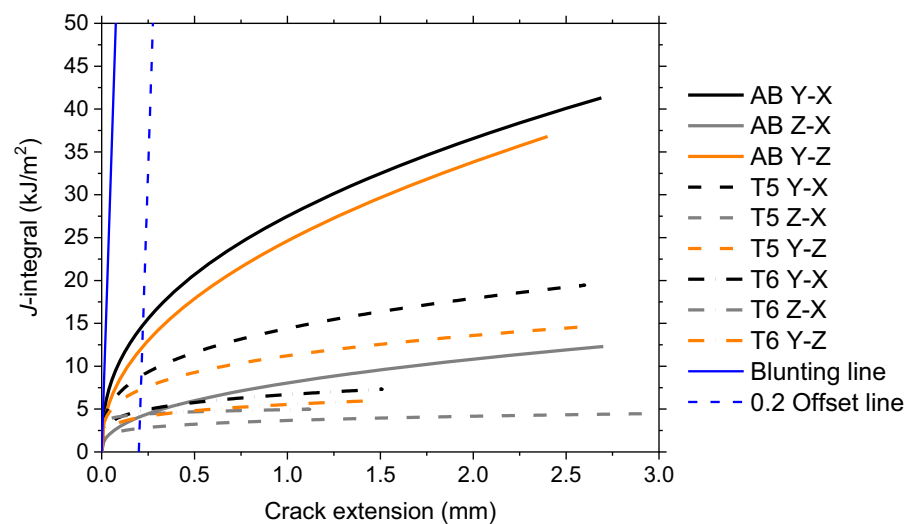


**Table 5**  $J_{Ic}$  values [kJ/m<sup>2</sup>] of the A357 Al alloy specimens for the three conditions

Orientation	Condition		
	AB	T5	T6
Y-X	14.83	8.88	4.77
Z-X	4.10	2.75	4.38
Y-Z	12.23	7.31	4.03

refined grain structure generated by the high cooling rates can be seen at the melt pool boundaries. On the other hand, at the central part of the melt pools, columnar grains are visible. The EBSD orientation map (Fig. 5a) show that the columnar grains grow along the building orientation without an evident preferred crystallographic orientation. In the AB condition, the microstructure consists of grains

composed by a sub-micrometer structure made of elongated cells decorated at boundaries by fine eutectic Al-Si network. In the T5 temper condition, the artificial ageing promotes a small coarsening of  $\alpha$ -Al grains surrounded by Si particles, and the precipitation of lath-shaped  $\beta''$  ( $Mg_4Al_3Si_4$ ) particles in the Al matrix (Fig. 3a, b). The T6 thermal treatment induces the coarsening of the microstructure produced by the SLM process, generating globular Si particles mainly at the grain boundaries of Al grains and micro-sized Si particles dispersed in the Al matrix, as can be seen in Fig. 4. The ageing in the T6 alloy also produces a fine dispersion of  $\beta''$  precipitates as shown in Asghar et al. (2020). A comparison, using Fig. 5 as a reference, indicates that no significant changes from the point of view of the texture are present before and after the T6 temper.

These microstructural differences affect the tensile properties (Table 4). In the AB condition, the sub-

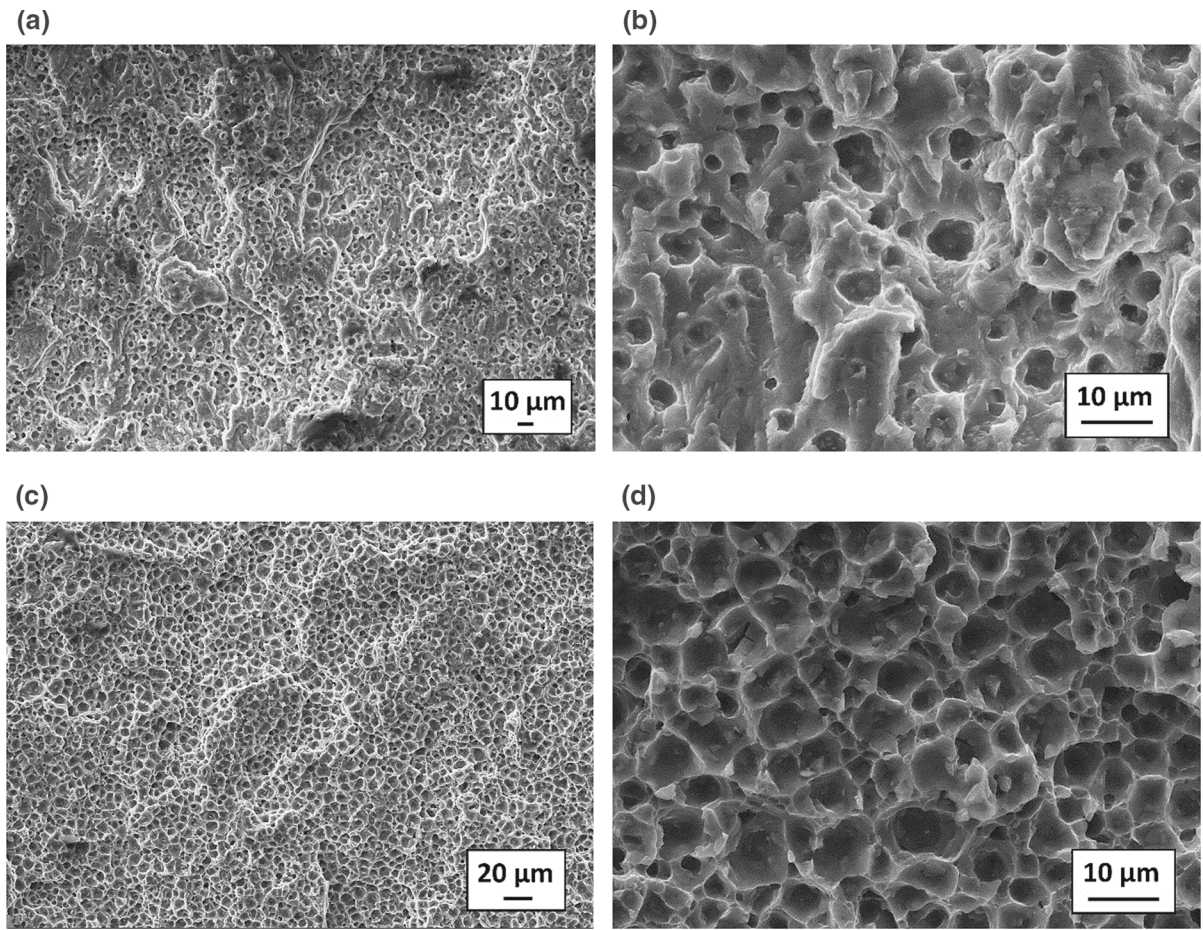


**Fig. 12** Fracture surface images taken by SEM of the T6 Z-X C(T) specimen. The fatigue pre-cracked region with magnification of: **a**  $\times 1000$ ; and **b**  $\times 5000$ ; the stable crack-growth region with magnifications of: **c**  $\times 1000$ ; and **d**  $\times 5000$

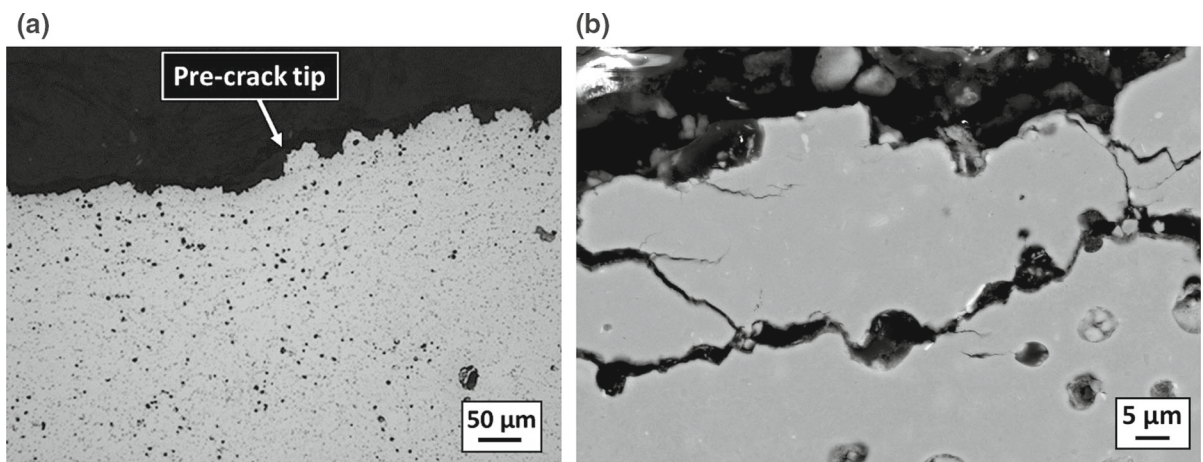


**Fig. 13 a** LOM micrograph taken from the mid-sections perpendicular to the crack plane showing the fatigue pre-crack and the stable crack-growth regions of the T6 Y-Z specimen

( $\times 200$ ). **b** SEM image from the mid-section perpendicular to the crack plane in the stable crack-growth region for the T6 Y-Z specimen ( $\times 3000$ )

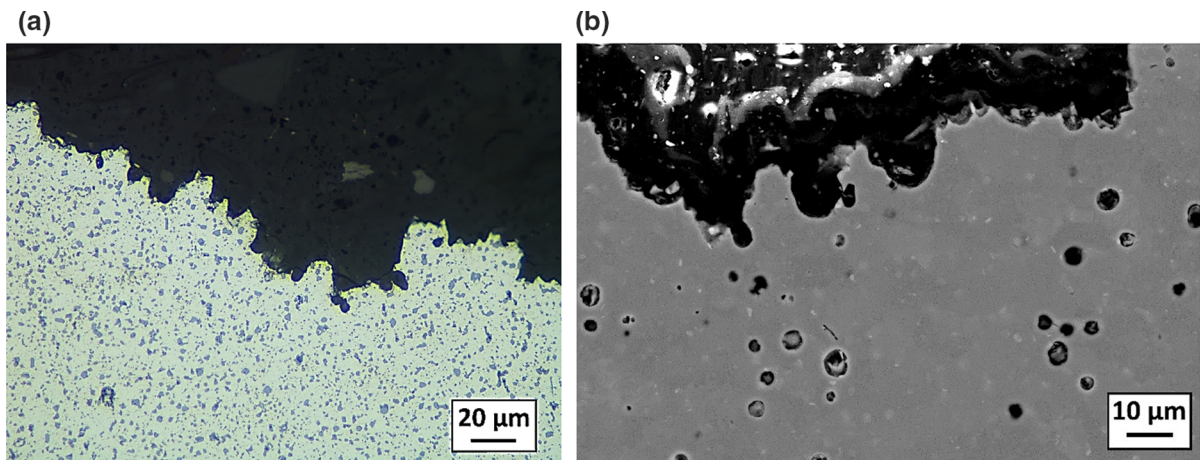


**Fig. 14** **a** LOM ( $\times 200$ ) and **b** SEM ( $\times 2000$ ) micrographs from the mid-section perpendicular to the crack plane in the stable crack-growth region for the T6 Y-X specimen

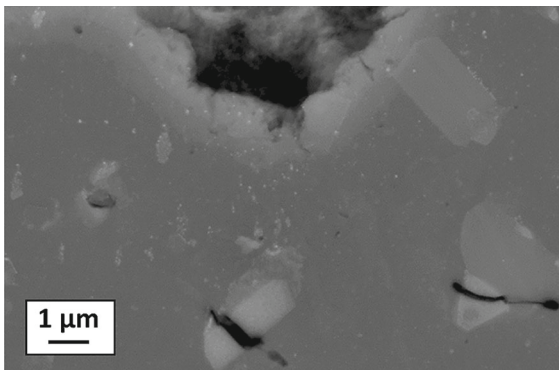


**Fig. 15** SEM image from the mid-section perpendicular to the crack plane in the stable crack-growth region for the T6 Y-X specimen ( $\times 20,000$ )

micrometer elongated cellular structure, parallel to building direction, was considered the main cause of the differences observed in the horizontal and vertical tensile specimens. Horizontal specimens featured higher  $\sigma_{YS}$  than the vertical ones, however similar  $\sigma_{UTS}$  values for both directions were observed indicating lower strain hardening effect in horizontal direction. In the T5 temper condition, the precipitation of the  $\beta''$  particles in the coarsened  $\alpha$ -Al grains surrounded by Si particles (elongated cellular structure) increased both  $\sigma_{YS}$  and  $\sigma_{UTS}$ . However, differences in  $\sigma_{YS}$  for the horizontal and vertical directions still exist, which could be related to the remaining elongated cellular structure. On the other hand, the T6 heat treatment reduced both the  $\sigma_{YS}$  and  $\sigma_{UTS}$  values when compared to the other conditions. It reduced also

the anisotropic behavior observed for the vertical and horizontal specimens of AB and T5 conditions considering the  $\sigma_{YS}$  values. Additionally, T6 temper reduced the strain hardening of the alloy, featuring the higher  $\sigma_{YS}/\sigma_{UTS}$  ratios in Table 4.

Regarding the fracture behavior of the material in the three conditions, the T6 thermal treatment reduced the highly anisotropic fracture behavior observed in the AB and T5 temper A357 Al alloy (Menezes et al. 2019). As can be seen in the last column of Table 5, T6 specimens featured similar fracture toughness values for all the crack orientations. Focusing on the effects of the microstructure on the fracture toughness, as can be seen in Fig. 4, in the T6 condition small Si particles are almost uniformly distributed inside the Al-matrix. As shown in Table 3, the average area of those particles is  $1.09 \pm 2.36 \mu\text{m}^2$ , the average aspect ratio is  $1.49 \pm 0.66$  and the average distance between the center of each particle is  $1.89 \pm 0.27 \mu\text{m}$ . Those features can be related to the fractographies presented in Fig. 12, where it is possible to observe very small dimples, some of them containing Si particles. The interface between these small and well distributed Si particles and the Al matrix seemed to act as microvoid starter reducing the fracture toughness of the alloy. Some fractured Si particles can be also seen near the crack path (Fig. 15). On the other hand, porosities also influenced the crack propagation path, as can be seen in Figs. 13 and 14. In the former figure, taken from the mid-section perpendicular to the crack plane in the stable crack-growth region for the T6 Y-Z

specimen, some small porosities are visible in the crack path. In addition, in the SEM image (Fig. 13b), some secondary cracks can be observed. In Fig. 14, where it is possible to observe the crack path from a LOM and SEM micrographs taken from the mid-section perpendicular to the crack plane of the T6 Y-X specimen, some small porosities can be seen along the crack propagation path. These facts indicate the porosities' effect in the crack propagation. Regarding the fracture toughness of the material in the T6 condition, the small uniformly distributed Si particles, and the porosities were considered the main causes for the low resistance to crack propagation. However, as both the micro-mechanisms occurred simultaneously during the tests, the individual contribution of each one on the resistance to crack propagation cannot be determined, as well as the independency or the possible interaction between them.

It is well known that the best materials for structural applications are those with good combinations of mechanical strength and fracture toughness. In this regard, Fig. 16 presents a plot of  $\sigma_{YS}$  against  $J_{Ic}$ ; from this figure it remains clear that the T6 condition featured the lowest average strength-toughness combination for all the tested orientations. On the other hand, one advantage of the T6 temper is the homogenization of the mechanical properties for the three orientations which makes this treatment attractive for applications where complex multiaxial stresses are present and a fair ductility is required (according to Table 4, T6 temper shows strains to failure higher than

6.8%, comparable to the AB condition and much higher than T5 temper). In addition, it is also important to highlight that the T6 temper removes the detrimental residual stresses induced by AM processes which are well known to play an important role in the structural integrity of AB parts and are responsible for part distortion after removal from the substrate. In its turn, the T5 temper is responsible for partially releasing the residual stresses, as shown in Casati et al. (2021). Another important observation is that the minimum  $J_{Ic}$  values for the AB and T5 conditions were determined along the Z-X orientation, with the lowest value associated with the T5 temper. This result suggests that loading the material in the building direction is not the best option both from the point of view of the tensile properties and the fracture toughness. The results presented in Fig. 16 also indicate that if toughness is important for the structural application, AB is the best condition (except for the Z-X crack orientation). If yield strength is the focus, T5 temper will be the best choice providing particular attention to the low toughness of the Z-X orientation and the general low ductility (strain to failure always lower than 5%).

After an extensive literature research, no data about the fracture response of the A357 alloy produced by LPBF in these three conditions were found. Comparisons with the tensile properties and fracture toughness data in the literature can be done only for castings. If further information is needed, data for Al-Si casting alloys are available in Tiryakioğlu (2008).

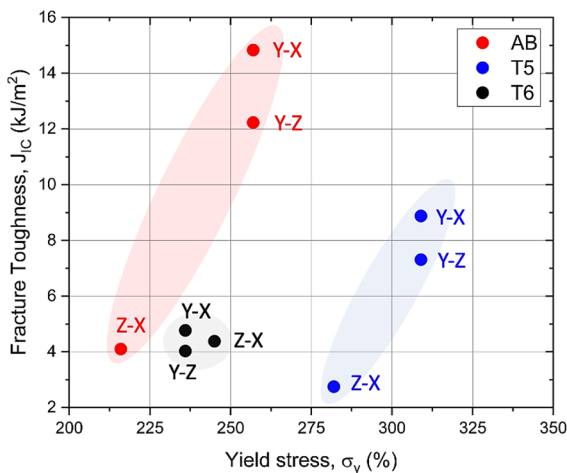


**Fig. 16** Experimental  $\sigma_{YS}$  vs.  $J_{Ic}$  for the A357 alloy in all conditions and crack propagation orientations

## 5 Concluding remarks

Based on the experimental results the following remarks can be made:

- Considering the specimen geometries employed in the present study, the material featured elastic–plastic (ductile) behavior for all conditions and crack orientations. The occurrence of ductile fracture was corroborated by the observation of the fracture surfaces.
- The mechanical anisotropy observed in both AB and T5 temper conditions were significantly reduced after T6 thermal treatment. However, in cases where the main loading direction is orthogonal to the building direction, the application of the

material in AB or T5 temper conditions should be considered. It is also worth noting that T6 treatment schedule is known to be able to relieve residual stresses, thus avoiding distortion or even failure of parts after removal from building platform, especially when dealing with large components.

- Except for cracks perpendicular to the building direction, the AB material featured the highest fracture toughness. The application of the AB material should be considered if fracture toughness is an important requirement for the application, and the main loading direction is not the building direction.
- Direct aging (T5 temper) increased both the  $\sigma_{YS}$  and  $\sigma_{UTS}$  of the as built material. This thermal treatment should be considered if tensile strength is important and cracks perpendicular to the building direction are not expected.
- The lowest mechanical properties for the AB and T5 conditions, both in terms of tensile strength and fracture toughness, are associated with loading along the building direction. This behavior was associated with the presence of preferential paths for crack growth along the melt pools boundaries.

**Acknowledgements** To the Italian Minister of Education for the scholarship of João Teixeira Oliveira de Menezes. The Italian Ministry of Education, University and Research is acknowledged for the support provided through the Project “Department of Excellence LIS4.0—Lightweight and Smart Structures for Industry 4.0”.

**Funding** Open access funding provided by Politecnico di Milano within the CRUI-CARE Agreement.

**Open Access** This article is licensed under a Creative Commons Attribution 4.0 International License, which permits use, sharing, adaptation, distribution and reproduction in any medium or format, as long as you give appropriate credit to the original author(s) and the source, provide a link to the Creative Commons licence, and indicate if changes were made. The images or other third party material in this article are included in the article’s Creative Commons licence, unless indicated otherwise in a credit line to the material. If material is not included in the article’s Creative Commons licence and your intended use is not permitted by statutory regulation or exceeds the permitted use, you will need to obtain permission directly from the copyright holder. To view a copy of this licence, visit <http://creativecommons.org/licenses/by/4.0/>.

## References

- Aboulkhair NT, Simonella M, Parry L, Ashcroft I, Tuck C, Hague R (2019) 3D printing of Aluminum alloys: additive manufacturing of aluminum alloys using selective laser melting. *Prog Mater Sci* 106:1–45
- Asghar G, Peng L, Fu P, Yuan L, Liu Y (2020) Role of Mg<sub>2</sub>Si precipitates size in determining the ductility of A357 cast alloy. *Mater Des* 186:1–9
- ASM Handbook (1992) Volume 2: Properties and selection: nonferrous alloys and special—purpose materials. American Society for Metals, Edition Metals Handbook
- ASTM E1820-20b (2020) Standard test method for measurement of fracture toughness. ASTM International, West Conshohocken
- ASTM E8/E8M-21 (2021) Standard test methods for tension testing of metallic materials. ASTM International, West Conshohocken
- BS 7448-1:1991, Fracture Mechanics Toughness Tests - Part 1: Method for determination of  $K_{Ic}$ , critical CTOD and critical J values of metallic materials, BSI – British Standards Institution, London, 2002 (corrigendum no. 1).
- BS EN ISO/ASTM 52900:2017 (2017) Additive manufacturing—General principles—Terminology. BSI—British Standards Institution, London (Corrigendum No. 1).
- Casati R, Vedani M (2018) Aging Response of an A357 Al alloy processed by Selective Laser Melting. *Adv Eng Mater* 21(4):1800406
- Casati R, Lemke J, Vedani M (2017) Microstructural and mechanical properties of as built, solution treated and aged 18 Ni 300 grade maraging steel produced by selective laser melting. *La Metall Ital* 1:11–20
- Casati R, Coduri M, Checchia S, Vedani M (2021) Insight into the effect of different thermal treatment routes on the microstructure of AlSi7Mg produced by laser powder bed fusion. *Mater Charact* 172:1–7
- DebRoy T, Wei HL, Zuback JS, Mukherjee T, Elmerb JW, Milewskic JO, Beesea AM, Wilson-Heida A, Ded A, Zhang W (2018) Additive manufacturing of metallic components—process, structure and properties. *Prog Mater Sci* 92:112–224
- Fiocchi J, Tuissi A, Biffi CA (2021) Heat treatment of aluminium alloys produced by laser powder bed fusion: a review. *Mater Des* 204:1–31
- Gu DD, Meiners W, Wissenbach K, Poprawe R (2012) Laser additive manufacturing of metallic components: materials, processes and mechanisms. *Int Mater Rev* 57(3):133–164
- ISO/ASTM52921-13 (2019) Standard Terminology for Additive Manufacturing—Coordinate Systems and Test Methodologies. ASTM International, West Conshohocken
- Marola S, Manfredi D, Fiore G, Poletti MG, Lombardi M, Fino P, Battezzati L (2018) A comparison of selective laser melting with bulk rapid solidification of AlSi10Mg alloy. *J Alloy Compds* 742:271–279
- Menezes JTO, Castrodeza EM, Casati R (2019) Effect of build orientation on fracture and tensile behavior of A357 Al alloy processed by Selective Laser Melting. *Mater Sci Eng A* 766:1–8
- Ninive PH, Strandlie A, Gulbrandsen-Dahl S, Lefebvre W, Marioara CD, Andersen SJ, Friis J, Holmestad R, Lovvik

- OM (2014) Detailed atomistic insight into the  $\beta''$  phase in Al-Si-Mg alloys. *Act Mater* 69:126–134
- Rao H, Giet S, Yang K, Wu X, Davies CHJ (2016) The influence of processing parameters on aluminum alloy A357 manufactured by selective laser melting. *Mater Des* 109:334–346
- Saboori A, Casati R, Zanatta A, Pavese M, Badini C, Vedani M (2018) Effect of graphene nanoplatelets on microstructure and mechanical properties of AlSi10Mg nanocomposites produced by hot extrusion. *Powder Metall Met Ceram* 56:647–655
- Tiryakiođlu M (2008) Fracture toughness potential of cast Al-7%Si-Mg alloys. *Mater Sci Eng A* 497:512–514
- Yang KV, Rometsch P, Davies CHJ, Huang A, Wu X (2018) Effect of heat treatment on the microstructure and anisotropy in mechanical properties of A357 alloy produced by selective laser melting. *Mater Des* 154:275–290

**Publisher's Note** Springer Nature remains neutral with regard to jurisdictional claims in published maps and institutional affiliations.